Mathematical Biology

Pulsations with reflected boundary waves: a hydrodynamic reverse transport mechanism for perivascular drainage in the brain

M. Coloma[1] · **J. D. Schaffer**[2] · **R. O. Carare**[3] ·
P. R. Chiarot[1] · **P. Huang**[1]

Abstract Beta-amyloid accumulation within arterial walls in cerebral amyloid angiopathy is associated with the onset of Alzheimer's disease. However, the mechanism of beta-amyloid clearance along peri-arterial pathways in the brain is not well understood. In this study, we investigate a transport mechanism in the arterial basement membrane consisting of forward-propagating waves and their reflections. The arterial basement membrane is modeled as a periodically deforming annulus filled with an incompressible single-phase Newtonian fluid. A reverse flow, which has been suggested in literature as a beta-amyloid clearance pathway, can be induced by the motion of reflected boundary waves along the annular walls. The wave amplitude and the volume of the annular region govern the flow magnitude and may have important implications for an aging brain. Magnitudes of transport obtained from control volume analysis and numerical solutions of the Navier–Stokes equations are presented.

✉ P. Huang
phuang@binghamton.edu

1 Department of Mechanical Engineering, State University of New York at Binghamton, 4400 Vestal Parkway East, Binghamton, USA

2 College of Community and Public Affairs, State University of New York at Binghamton, 4400 Vestal Parkway East, Binghamton, USA

3 Faculty of Medicine, University of Southampton, Southampton, UK

🌀 Springer

1 Introduction

Alzheimer's disease (AD) is the seventh leading cause of death in the United States (Alzheimer's Association 2010). The accumulation of beta-amyloid proteins (A β) in the vasculature walls of the brain is a characteristic of cerebral amyloid angiopathy (CAA) and AD (Preston et al. 2003). There is significant evidence suggesting that pathologies associated with A β clearance failure in the brain contribute to the occurrence of AD (Abbott 2004; Hawkes et al. 2011; Iliff et al. 2012; Mawuenyega et al. 2010; Tanzi et al. 2004; Weller et al. 2010). Known mechanisms for A β elimination from the brain include proteolltic degradation (Tanzi et al. 2004), receptor-mediated transport (Tanzi et al. 2004; Knopf et al. 1995), and flow in the perivascular structures (Carare et al. 2008; Iliff et al. 2012). However, the biomechanical mechanism of A β clearance in the perivascular structures remains unclear. Previous studies have suggested that pulsating blood vessels may be associated with A β clearance through this pathway (Hawkes et al. 2011; Iliff et al. 2012; Mawuenyega et al. 2010).

Several theoretical models of perivascular flow have been proposed and investigated (Bilston et al. 2003; Schley et al. 2006; Wang and Olbricht 2011). Bilston et al. (2003) modeled the flow along the perivascular space to determine whether local arterial pulsations are sufficient to transport cerebral spinal fluid (CSF) in the spinal cord. Their findings indicate that the CSF flows in the same direction as arterial pulsations even against an adverse pressure gradient. Wang and Olbricht (2011) modeled peristaltic motion on a porous perivascular pathway as a mechanism of interstitial fluid (ISF) transport. It is worth noting that both Bilston et al. (2003) and Wang and Olbricht (2011) focused on transport outside the blood vessels. In this study our interest is on modeling the transport pathway in the arterial basement membrane (ABM), which is part of the blood vessel wall.

Experimental evidence by Carare et al. (2008) and Hawkes et al. (2013) confirm that the ABM is a conduit for A β transport out of the brain while the arterial lumen provides oxygen-rich blood to the brain parenchyma. The ABM is within the arterial wall that is separated with multiple layers of smooth muscles cells (Carare et al. 2008). As shown in Fig. 1, it is postulated that the ISF in the ABM is transported in the *reverse direction* of blood flow (Carare et al. 2008). Several mechanisms of A β clearance in the reverse direction were proposed by Schley et al. (2006). One mechanism was the existence of global pressure differences in the brain. However, this mechanism could not explain preferential drainage in the ABM because ISF could also flow in the para-venous pathways. Another mechanism considered was that drainage can be achieved by A β actively adhering to and detaching from the walls of the ABM to yield a one-way valve-like effect during each pulse cycle (Schley et al. 2006). Still, this mechanism does not explain the observation of passive soluble tracers traveling in the reverse direction through the ABM (Carare et al. 2008). This leads us to believe that the transport in the ABM is perhaps facilitated by a hydrodynamic mechanism.

Iliff et al. (2013) reported measurements on wave pulsations along brain penetrating arteries/arterioles and Hughes et al. (2014) and Weller et al. (2008) suggested wave reflection may be a critical mechanism for A β clearance. In this paper, we investigate a preferential transport theory where reverse transport is hydrodynamically driven by the superposition of forward-propagating waves and their associated wave reflections
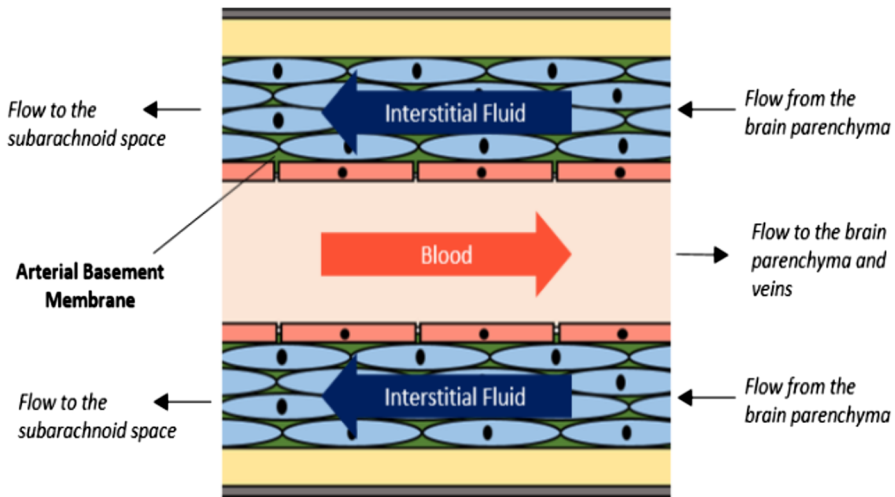
Fig. 1 A diagram depicting the axial view of a cerebral artery, the direction of blood flow, and the reverse ISF flow in the ABM. The ABM is between the layers of smooth muscle cells that are depicted as ovals

along the arterial lumen. The forward-propagating waves are generated by the pulsation of the heart, while the reflection waves are created at the arterial branching junctions or any other sites with sudden changes in arterial geometry and/or elastic properties (Alastruey et al. 2012; Papageorgiou et al. 1990). Our model helps predict the lack of ISF drainage following cardiac arrest in mice (Carare et al. 2008) and incorporates physiological relevant parameters based on the extensive literature available for reflected boundary waves in blood vessels (Fung 1984; Li 2004; Nichols et al. 2011). We analyzed the direction of perivascular flow under various wave conditions via a hydrodynamic control volume analysis and corroborated the results with the Navier–Stokes equations numerically solved by the finite volume method. These modeling tools also provided a means for us to gain insights into how the peri-arterial transport can be adversely affected by aging abnormalities such as basement membrane thickening (Farkas and Luiten 2001) and an increase in arterial wall stiffness (Nichols 2005).

2 Theoretical considerations

2.1 Direction of overall flow through a periodically deforming annulus

We model the ABM as an axisymmetrical annulus between concentric cylinders of equal length l (Fig. 2), which is equal to the distance between two arterial bifurcation points. We assume that the lateral surfaces of the annulus are impermeable to the fluid, and thus the overall fluid transport is only in the axial direction, x. The incompressible ISF in the annulus has a water-like density of 1000 kg/m^3 and a viscosity of 0.0035 kg/m s^{-1} (Yao et al. 2012). In the unperturbed state (Fig. 2a), the annulus is defined by radii b_i and b_o, where the subscripts i and o indicate the inner and outer
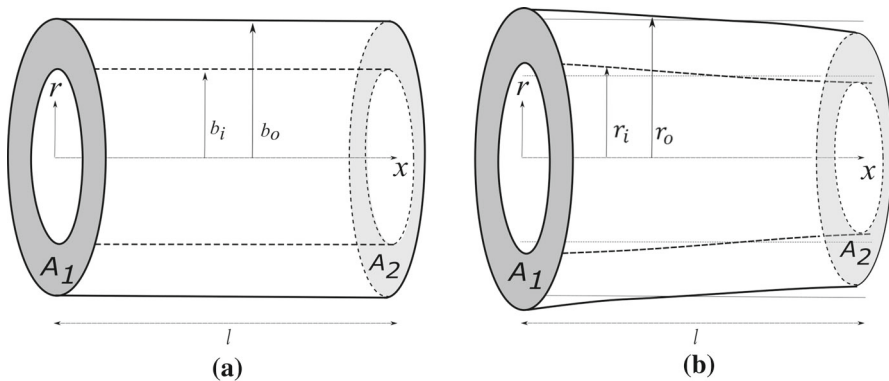
Fig. 2 Depiction of an annulus with two openings A_1 and A_2 at $x = 0$ and $x = l$, respectively. **a** An unperturbed annulus; **b** a deformed annulus at an instant in time with $A_1 > A_2$

lateral surfaces, respectively. The end openings of the annulus have cross-sectional areas A_1 and A_2, where the subscripts 1 and 2 indicate location at $x = 0$ and $x = l$, respectively. As shown in Fig. 2b, a traveling boundary wave causes the annulus to deform and its cross-sectional area to vary in both x-position and time, t.

It is anticipated that the overall flow magnitude and direction are the integrated effect of the rate of change of the annular volume and the instantaneous cross-sectional area ratio between the two annular openings, $\alpha \equiv A_2/A_1$. Given that the ISF is an incompressible fluid, the rate of change of the annular volume provides the driving force for fluid motion. That is, without expansion or compression of the annular region, the flow rates at A_1 and A_2 should be zero. On the other hand, α determines the instantaneous overall flow direction as a larger flow magnitude can be found at the larger opening where the flow resistance is lower, given that the flow resistance is inversely proportional to the cross-sectional area squared. Figure 3 demonstrates the preferential flow direction of an incompressible fluid under different scenarios of annular volume changes and values of α. In Fig. 3a, b an *expanding* annulus causes the fluid to *enter* the annular region. If $\alpha < 1$, more fluid enters at A_1 than at A_2 and consequently the overall flow direction is $+x$ (Fig. 3a); if $\alpha > 1$ more fluid enters A_2 and the overall flow direction is reversed (Fig. 3b). Similar inference can also be made for the overall flow direction when the annular volume is *contracting* and the fluid inside *exits* the annular region (Fig. 3c, d). Therefore, an overall reverse flow through the annulus can be obtained if a surface deformation cycle consists of longer durations of the scenarios depicted in Fig. 3b, d than the ones depicted in Fig. 3a, c. In the following sections, we present examples that exhibit the characteristics of motion associated with Fig. 3b, d that generate a reverse flow.

2.2 Boundary waves

The traveling waves are prescribed as radius functions $r_i(x, t)$ and $r_o(x, t)$. We assume that wave reflections can occur on the outer and inner lateral surfaces at $x = 0$ and

	Net Forward Flow	Net Reverse Flow
Expanding Volume	(a)	(b)
Contracting Volume	(c)	(d)
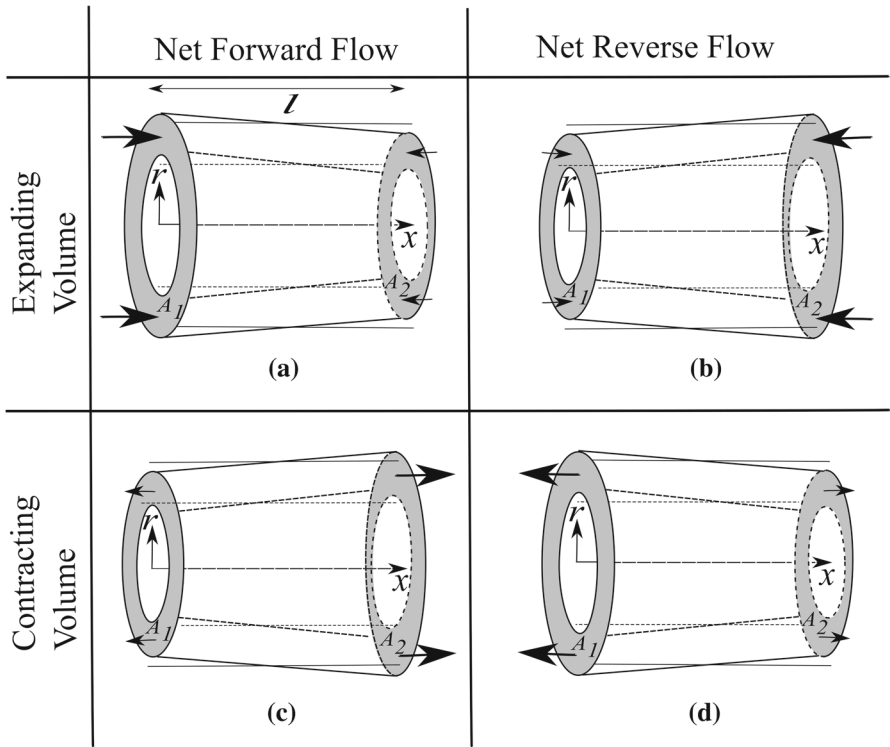
Fig. 3 Schematics of preferential flows in an axisymmetric annulus with length l under the four possible types of deformation. The cross-sectional areas A_1 and A_2 are located at $x = 0$ and $x = l$, respectively. **a** Expanding annular volume ($dV/dt > 0$) with $\alpha < 1$, **b** expanding annular volume ($dV/dt > 0$) with $\alpha > 1$, **c** contracting annular volume ($dV/dt < 0$) with $\alpha > 1$, **d** contracting annular volume ($dV/dt < 0$) with $\alpha < 1$. V represents the instantaneous volume of the annulus and $\alpha = A_2/A_1$. The size of the *arrows* is indicative of the instantaneous flow rate

$x = l$ which are the vessel bifurcation sites with a local stiffness discontinuity. All waves on both lateral surfaces are assumed to have the same wave number, k, and angular frequency, ω. The amplitudes of the heart driven forward propagating pulse wave on both lateral surfaces are assumed to be a. These waves are non-dispersive and undamped during propagation. Assuming that the waves take the form of sinusoidal functions, the outer and inner annular surfaces can be described by:

$$r_o(x, t) = a \, \text{Re} \left\{ \sum_{n=0}^{M-1} \left[R_{2,o} R_{1,o} \exp(2ikl) \right]^n \exp(-i\omega t) \left[\exp(ikx) \right. \right.$$

$$\left. \left. + R_{2,o} \exp(-ikx + 2ikl) \right] \right\} + b_o \tag{1}$$

$$r_i(x, t) = a \, \text{Re} \left\{ \sum_{n=0}^{M-1} \left[R_{2,i} R_{1,i} \exp(2ikl) \right]^n \exp(-i\omega t) \left[\exp(ikx) \right. \right.$$

$$+R_{2,i} \exp(-ikx + 2ikl) \Bigg] \Bigg\} + b_i \tag{2}$$

where M is an integer greater than or equal to 1. $R_{1,o}$ and $R_{2,o}$ are the wave reflection coefficients for the outer lateral wall at $x = 0$ and $x = l$, respectively; $R_{1,i}$ and $R_{2,i}$ are the wave reflection coefficients for the inner lateral wall at $x = 0$ and $x = l$, respectively. All reflection coefficients must have numerical values between -1 and 1. Equations (1) and (2) each represents a forward-propagating wave superimposed with wave reflections between $x = 0$ and $x = l$, and $2M - 1$ is the total number of wave reflections (Fig. 4).

For $M = 1$ (Fig. 4a), the forward-propagating wave is reflected at $x = l$. The reflected wave propagates in the negative x-direction with a smaller amplitude (i.e.
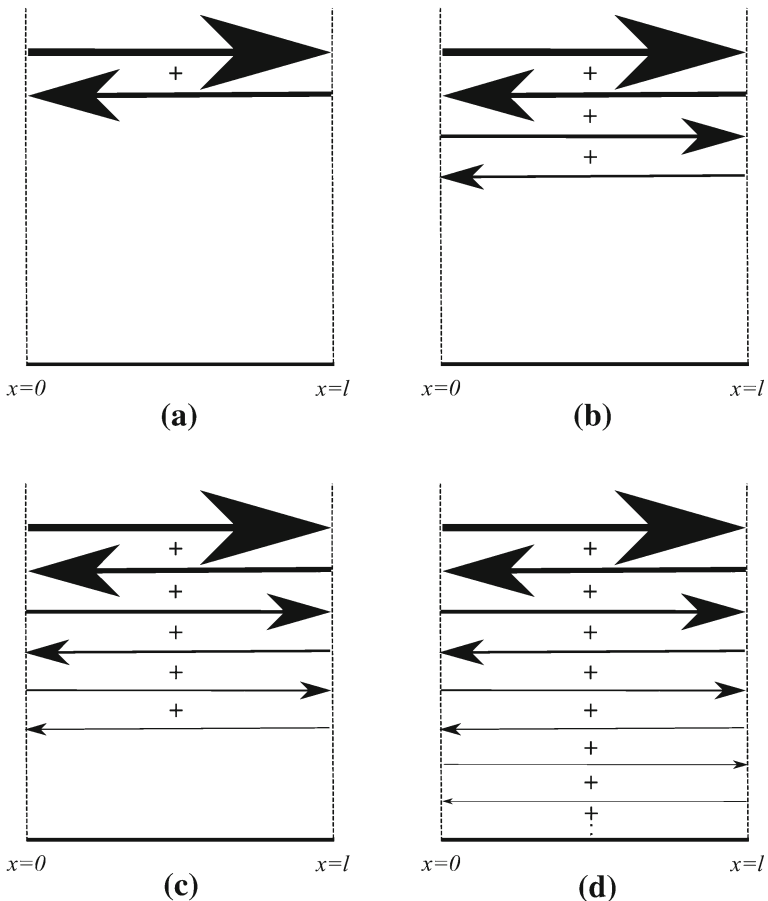
Fig. 4 Wave reflections on the inner and/or outer lateral surface for **a** $M = 1$, **b** $M = 2$, **c** $M = 3$, and **d** $M \to \infty$. Transverse waves travel in the positive and negative x-directions, with reduced wave amplitude after each reflection. The size of each *arrow* is indicative of the wave amplitude, and the *plus signs* graphically represent wave superposition

$R_{2,o} \cdot a$ and $R_{2,i} \cdot a$), and no wave reflection is assumed at $x = 0$. Under this scenario, Eqs. (1) and (2) reduce to

$$r_o(x, t) = a \operatorname{Re} \left\{ \exp\left(-i\omega t\right) \left[\exp(ikx) + R_{2,o} \exp(-ikx + 2ikl) \right] \right\} + b_o \quad (3)$$
$$r_i(x, t) = a \operatorname{Re} \left\{ \exp\left(-i\omega t\right) \left[\exp(ikx) + R_{2,i} \exp(-ikx + 2ikl) \right] \right\} + b_i. \quad (4)$$

For $M = 2$, the wave reflects once at $x = 0$ and twice at $x = l$, and the annular deformation consisting of the base forward-propagating wave superimposed with three reflected waves as shown in Fig. 4b. Finally, one can consider an infinite number of reflections ($M \to \infty$) as the waves bounce between $x = 0$ and $x = l$ (Fig. 4d), and thus Eqs. (1) and (2) become

$$r_o(x, t) = a \operatorname{Re} \left\{ \frac{1}{1 - R_{2,o} R_{1,o} \exp\left(2ikl\right)} \exp\left(-i\omega t\right) \right.$$
$$\left. \times \left[\exp(ikx) + R_{2,o} \exp(-ikx + 2ikl) \right] \right\} + b_o, \quad (5)$$

$$r_i(x, t) = a \operatorname{Re} \left\{ \frac{1}{1 - R_{2,i} R_{1,i} \exp\left(2ikl\right)} \exp\left(-i\omega t\right) \right.$$
$$\left. \times \left[\exp(ikx) + R_{2,i} \exp(-ikx + 2ikl) \right] \right\} + b_i. \quad (6)$$

The reflection coefficients are independent non-dimensional parameters. Their values depend on the local wave medium discontinuity due to changes in mechanical and/or geometric properties. When a reflection coefficient is positive, the reflected wave is in phase with the incident wave. On the other hand, a negative reflection coefficient indicates that the reflected wave is 180 degrees out of phase from the incident wave (Elmore and Heald 1969). The arterial stiffness increases longitudinally towards capillaries (Hughes et al. 2014). In wave physics, a wave traveling from a less stiff into a stiffer medium results in a negative reflection coefficient at the junction point. Therefore, we enforce the conditions that $R_{1,o}$, $R_{1,i} > 0$ and $R_{2,o}$, $R_{2,i} < 0$, where we assume that the arterial segment bifurcates into smaller arterioles at $x = l$.

2.3 Control volume analysis

The most significant advantage of using a control volume analysis is that it can provide the overall flow direction and an estimated magnitude of flow rate within a fraction of the computational time needed to numerically solve the Navier–Stokes equations. This provides us with a convenient tool to assess the required boundary wave conditions needed to generate reverse transport. In our results section, we will show that the control volume analysis qualitatively agrees with the computation-intensive Navier–Stokes equations solution.

We define the control volume as the periodically deforming annulus with two open control surfaces as illustrated in Fig. 2. For an incompressible and homogenous fluid,

the conservation of mass and momentum equations for a control volume reduces to

$$\rho \frac{dV}{dt} = \rho \bar{u}_1 A_1 - \rho \bar{u}_2 A_2 \tag{7}$$

$$\frac{d}{dt}(\rho P) = \rho \beta_1 \bar{u}_1^2 A_1 - \rho \beta_2 \bar{u}_2^2 A_2 \tag{8}$$

where V is the volume of the annular segment, $\bar{u}$ is the average cross-sectional fluid velocity in the x-direction, β is the momentum-flux correction factor, ρ is the fluid density, and ρP is the total x-direction linear momentum inside the control volume. For our annulus with radii $0.33 \leq r_i/b_o \leq 0.83$ and $0.83 \leq r_o/b_o \leq 1.17$, it is found that $\beta_{1,2} = 1.20 \pm 0.01$ (Appendix 1). Thus, during all control volume analysis computations, we set $\beta_1 = \beta_2 = 1.20$. Given that $\bar{u}_1$ must remain real, periodic, and finite, a series of binomial expansion of Eqs. (7) and (8) leads to an approximate formula for the overall volume of fluid transported per wave period (Appendix 2),

$$Q_{CV} \approx \frac{\int_0^\tau \frac{dV}{dt} \frac{1}{(1+\alpha^{1/2})} dt}{1 - \frac{1}{2\beta_1 \int_0^\tau A_1(t)dt} \int_0^\tau A_1 \alpha^{1/2} dt} \tag{9}$$

where τ is the wave period. The calculations of V, A_1, and α were carried out using the prescribed boundary waves given in Eqs. (3) to (6) while numerical integration of Eq. (9) was performed using the quadrature method with a tolerance of 10^{-6}.

2.4 Numerical solutions of the Navier–Stokes equations for laminar, incompressible flow

In addition to the control volume analysis, the flow magnitude can also be obtained through solutions to the coupled continuity and Navier–Stokes equations,

$$\nabla \cdot \mathbf{u} = 0 \tag{10}$$

$$\rho \frac{D\mathbf{u}}{Dt} = -\nabla p + \mu \nabla^2 \mathbf{u} \tag{11}$$

where $\mathbf{u}$ is the flow velocity field, μ is the fluid viscosity, and the effect of gravity is assumed negligible. We used the finite volume method-based ANSYS FLUENT 15.0 to solve the Navier–Stokes and the continuity equations and obtained instantaneous velocity fields inside the annulus during periodic volume deformation. The governing equations were solved iteratively until the scaled residuals of continuity and velocity became less than 10^{-12} and 10^{-15}, respectively. A no-slip boundary condition was imposed on the inner and outer lateral surfaces while they deform according to Eqs. (3) to (6). Pressures at the annular openings were set to zero and the fluid was initially at rest.

To accommodate the deforming annulus we used the diffusion-based smoothing method to update the finite volume mesh during each time step. In ANSYS FLUENT, this method moves mesh nodes in response to the displacement of the boundaries by solving the diffusion equation for mesh velocities. The velocity at a boundary node

is considered as a Dirichlet boundary condition. The diffusion equation is discretized using the standard finite volume method and solved iteratively using the algebraic multigrid solver. By default, the number of iterations and relative residual tolerance for solving the mesh motion equation are 20 and 10^{-4}, respectively. Other moving mesh algorithms such as dynamic layering and remeshing methods were considered but ultimately not adopted. Dynamic layering allows the addition or removal of cell layers adjacent to the moving boundary based on its height. We did not choose dynamic layering because our prescribed deformation varies in the axial direction, and thus the adjacent cell height layer is not uniform and compromises the mesh quality. Remeshing methods require a triangular mesh, which we found to provide poorer convergence than a structured grid with quadrilateral elements.

The simulations were performed for a time duration of eight wave periods. The overall fluid volume transported over a wave period, Q_{NS}, is obtained by

$$Q_{NS} \equiv \int_{t}^{t+\tau} \left\{ \int_{r_i(t')}^{r_o(t')} \left[u_1(r, t') \cdot \hat{x} \right] 2\pi r \, dr \right\} dt' \tag{12}$$

All simulations show Q_{NS} during the seventh and the eighth wave periods differed by less than 0.01 %, which suggests that during the eighth period the annular flow had reached a periodic state.

Our mesh consisted of 42,021 nodes and we chose a time step size of $\Delta t = 0.01$ s. The mesh sensitivity of the simulations was determined by varying the number of nodes in the annulus and comparing Q_{NS}. For the same annular volume, the number of nodes was varied from 11,021 to 164,041 while maintaining $\Delta t = 0.01$ s. Within this range of grid resolution, Q_{NS} was found to change by less than 0.2 %, which indicates that the lower mesh density was sufficient. The time step size sensitivity was evaluated by varying Δt between 0.02 and 0.005 s and comparing Q_{NS} while keeping the number of nodes fixed to 42,021. We confirmed that Q_{NS} changes by less than 0.50 %, which suggests that a relatively larger time step size can be used for computational efficiency.

3 Results and discussion

3.1 Non-dimensional parameters

The characteristic lengths of the simulations are $b_o = 40$ μm (radial) and $l = 2$ mm (longitudinal), while the characteristic time is the wave period, $\tau = 1$ s, which is based on the human heart rate. Non-dimensional independent parameters $\tilde{a}$, $\tilde{k}$, $\tilde{b}_i$, and $\tilde{\omega}$ are referred to as the amplitude-to-radius ratio, the non-dimensional wave number, the radius ratio, and the non-dimensional wave frequency, respectively. $\tilde{a} \equiv a/b_o \sim 0.1$ is based on the arterial wave amplitude (Yang et al. 1991) and radius (Li 2004) measurements reported in the literature. Here, $\tilde{k} \equiv kl \sim 0.01$ and ~ 0.001 are for the arteries and the arterioles, respectively, based on the measured pulse wave speed (Li 2004; Knopf et al. 1995) and blood vessel length (Li 2004; Kamath 1981). $\tilde{b}_i \equiv b_i/b_o$ is between 0.6 and 0.8 based on reported outer mean radius and wall thickness measurements (Li 2004; Krings et al. 2011) while $\tilde{\omega} \equiv \tau\omega = 2\pi$. The non-
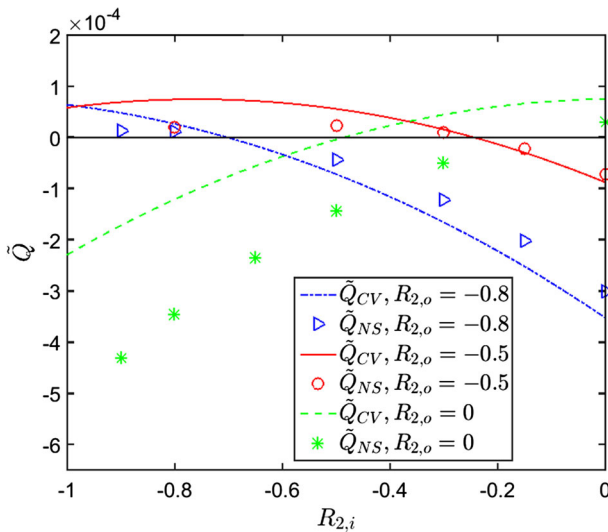
Fig. 5 The fluid volume transported per wave period, $\tilde{Q}$, versus $R_{2,i}$ with $M = 1$ and for different values of $R_{2,o}$. $\tilde{Q}_{CV}$ is obtained from the control volume analysis while $\tilde{Q}_{NS}$ is obtained from the numerical solutions of the Navier–Stokes equations. All data have the same parameter values of $\tilde{a} = 1/12$, $\tilde{k} = \pi/500$, and $\tilde{b}_i = 2/3$

dimensional fluid volume transported per wave period is $\tilde{Q} \equiv Q/b_o^2 l$. The Reynolds number is much less than 1 for all cases, rendering the flow laminar throughout.

3.2 Wave reflections on the inner and outer lateral surfaces

Wave reflections may occur on both the inner and outer lateral surfaces of the ABM, and both scenarios are accounted for in our model. Figure 5 shows the net flow $\tilde{Q}$ for varying $R_{2,o}$ and $R_{2,i}$. A positive value of $\tilde{Q}$ indicates a net forward flow (in the same direction as the blood flow), while a negative $\tilde{Q}$ represents an induced reverse flow in the annulus. Our results show that the reflection coefficients on the inner and outer lateral surface must be mismatched in order to obtain a significant reverse flow. For example, to create a large net reverse flow, $R_{2,o}$ should be close to -1 and $R_{2,i}$ should be close to 0 (or vice versa). In other words, to drive flow in the reverse direction, the boundary deformations must be incoherent on the inner and outer surfaces. If the boundary deformations are similar (i.e. when the reflection coefficients are closely matched), the flow is driven in the forward direction or is completely inhibited. Physiologically, mismatched reflection coefficients are expected given the variation in material properties on the inner and outer lateral surfaces of the arterial lumen. To highlight the importance of the key parameters (e.g. $R_{1,o}$, $R_{2,o}$, $\tilde{k}$, $\tilde{b}_i$) on $\tilde{Q}$, in the following sections we mainly focus on the case where a large reverse flow is possible; i.e. when $R_{2,i} \neq R_{2,o}$.

3.3 The effects of $R_{1,o}$, $R_{2,o}$, and $\tilde{k}$ on the flow

Our results indicate that the reflection coefficients, $R_{1,o}$ and $R_{2,o}$, strongly influence the overall transport direction, while the transport magnitude depends on $\tilde{k}$. Figure 6 shows the fluid volume transported per wave period, $\tilde{Q}$, for annular deformation under $M = 1$ (Eqs. (3) and (4)). Here, our computational results predict that when $\tilde{k} << 1$, reverse transport occurs only for $R_{2,o} < -0.33$. This finding can be understood by considering our preferential flow theory (Fig. 3). In Fig. 7, we plot $d\tilde{V}/d\tilde{t}$ verses $\tilde{t}$ along with α verses $\tilde{t} \equiv t/\tau$ where $\tilde{V} \equiv V/b_o^2 l$. The regions that are shaded represent the time duration when $d\tilde{V}/d\tilde{t} > 0$ and $\alpha > 1$ (Fig. 3b) or $d\tilde{V}/d\tilde{t} < 0$ and $\alpha < 1$ (Fig. 3d). These are the conditions that are favorable to reverse fluid flow. It can be seen that the larger the value of $|R_{2,o}|$, the longer these favorable conditions last, and thus the greater the reverse transport. For example, at $R_{2,o} = 0$ (Fig. 7a), the favorable conditions never occur, and thus no reverse transport is observed. At $R_{2,o} = -0.4$ (Fig. 7b), the favorable annular deformation conditions occur 72.3 % of the time during a wave period, resulting in an overall reverse transport. For $R_{2,o} = -0.8$ (Fig. 7c), the favorable conditions occur 99.8 % in each wave period, thus leading to a very strong reverse flow in the annulus (i.e. for this case, the reflection coefficients are highly mismatched).

From a physical point of view, $|R_{2,o}|$ represents the relative amplitude or strength of the reflected wave as compared to the forward propagating wave. At $-0.33 \leq R_{2,o} < 0$ the reflected wave is simply too weak to overpower the forward moving wave to create a reverse flow in the annulus. It is also interesting to note that a reverse flow does not require the reflected wave to be as strong as the forward moving wave. For example, a reflected wave that has only half the amplitude as the forward wave ($R_{2,o} = -0.5$) is already capable of inducing a reverse flow in the annulus. Of course, the larger the value of $|R_{2,o}|$, the stronger the reverse transport.

The value of the non-dimensional wave number $\tilde{k}$ is found to affect the transport magnitude, but not direction. Decreasing $\tilde{k}$ from $\pi/250$ to $\pi/1000$ leads to a decrease in the flow magnitude. When $\tilde{k}$ becomes smaller, the annulus occupies a smaller fraction of the wavelength at any instant of time, and consequently, the difference between A_1 and A_2 also becomes smaller. In other words, one expects that α is a monotonically increasing function of $\tilde{k}$ and $\alpha(t, \tilde{k} \rightarrow 0) \rightarrow 1$. Since the magnitude of transport is related to the value of α integrated over time, a decrease in $\tilde{k}$ lowers the overall flow magnitude (Fig. 6).

We next turn our attention to the case where the traveling waves can reflect at both $x = 0$ and $x = l$ (i.e. $M \rightarrow \infty$). The key difference here is that the value of $R_{1,o}$ also determines the transport magnitude. In Fig. 8, we plot $R_{1,o}$ verses $\tilde{Q}$ for different values of $R_{2,o}$. As before, when $|R_{2,o}|$ increases, the magnitude of the overall reverse flow increases. Our model also indicates that once $|R_{2,o}|$ determines the transport direction, $R_{1,o}$ can change the flow magnitude but cannot influence the flow direction. Our computation shows that $|R_{2,o}| > 0.5$ is needed for peri-arterial drainage out of the brain regardless of the value of $|R_{1,o}|$.
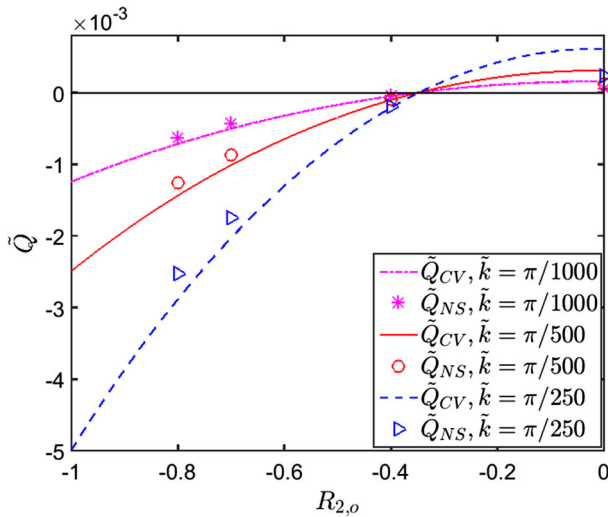
Fig. 6 The fluid volume transported per wave period, $\tilde{Q}$, versus $R_{2,o}$ for $M = 1$. $\tilde{Q}_{CV}$ is obtained from the control volume analysis while $\tilde{Q}_{NS}$ is obtained from the numerical solutions of the Navier–Stokes equations. All data have the same parameter values of $R_{2,i} = 0$, $\tilde{a} = 1/6$, and $\tilde{b}_i = 2/3$

3.4 Transport implications for an aging brain

An aging brain is characterized by the thickening of the ABM (Farkas and Luiten 2001) and stiffening of the arterial wall (Nichols 2005). Here, we interpret the ABM thickening as increasing the gap size, $\tilde{h}$, of the annulus where $\tilde{h} = 1 - \tilde{b}_i$, which is manifested through decreasing the value of $\tilde{b}_i$. The arterial stiffening is interpreted as the vessel wall becoming less elastic, resulting in a smaller traveling wave amplitude, $\tilde{a}$. Given that multiple wave reflections are found to not impact the overall fluid transport direction, here we first focus on computational cases where $M = 1$ to obtain some physical understanding.

In Fig. 9, we plot $\tilde{Q}$ versus $R_{2,o}$ for three different scenarios of the aging brain. In Fig. 9a, we observe that $\tilde{Q}$ shifts upward when $\tilde{b}_i$ decreases. That is, an increase in the annular gap size $\tilde{h}$ causes the overall fluid transport to become more positive: a flow that is originally in the reverse direction becomes weaker in magnitude, while an originally forward flow becomes stronger. This can be explained by comparing Fig. 10a with Fig. 7c, both of which are plotted with identical parameter values except $\tilde{b}_i$. It can be observed that when $\tilde{b}_i$ changes from 2/3 to 1/2, the duration of favorable conditions for reverse flow (shaded regions) reduced in each wave period, thus reducing the magnitude of the reverse transport. Furthermore, under certain range of $R_{2,o}$ the flow can even change direction. For example in Fig. 9a, at $R_{2,o} = -0.4$, transport in the annulus goes from reverse for $\tilde{b}_i = 2/3$ to forward for $\tilde{b}_i = 1/2$. Again, our understanding of the duration of favorable conditions for reverse flow provides the physical reasoning behind this observation. For $\tilde{b}_i = 2/3$ (Fig. 7b), the favorable conditions are seen to last much longer per wave period than the case of $\tilde{b}_i = 1/2$ (Fig. 10b). Overall, this suggests a potential mechanism to explain how aging arteries
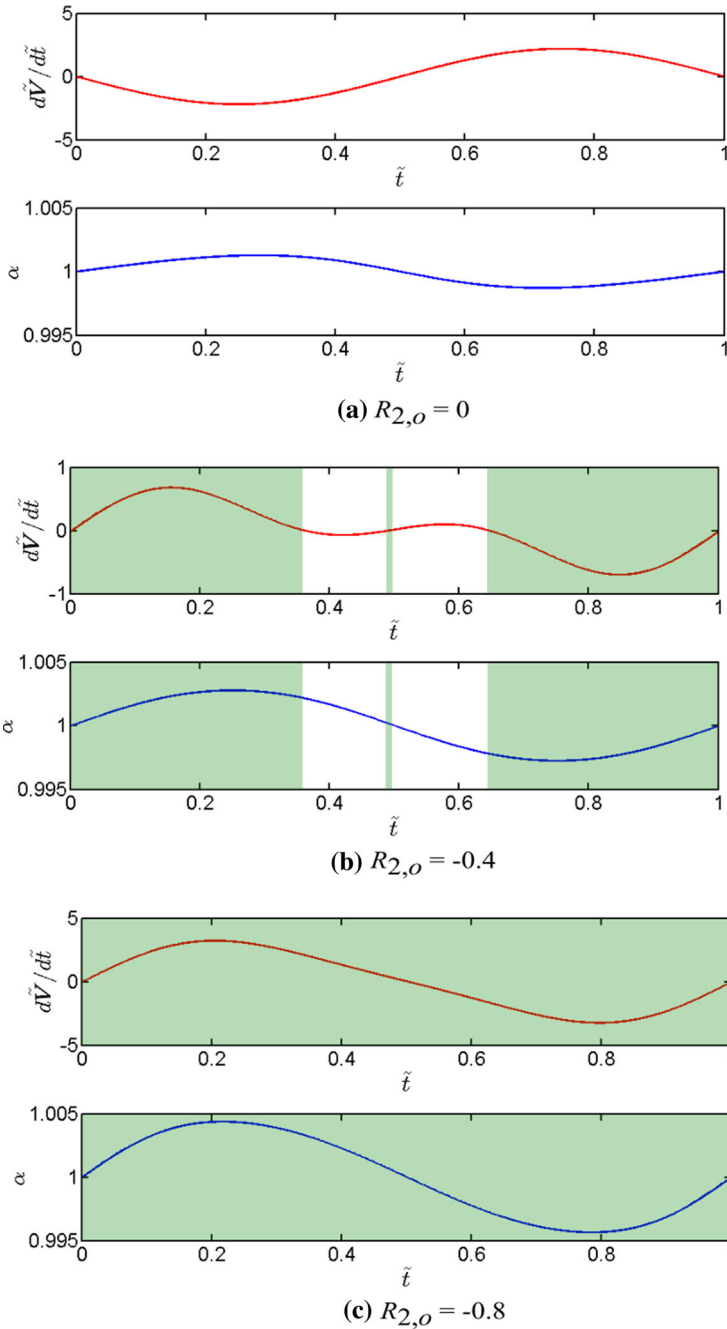
Fig. 7 $d\tilde{V}/d\tilde{t}$ verses $\tilde{t}$ and α verses $\tilde{t}$ with parameter values of $M = 1$, $R_{2,i} = 0$, $\tilde{a} = 1/6$, $\tilde{b}_i = 2/3$, and $\tilde{k} = \pi/500$. **a** $R_{2,o} = 0$; **b** $R_{2,o} = -0.4$; **c** $R_{2,o} = -0.8$. The *shaded* regions indicate the time intervals of favorable conditions for reverse flow
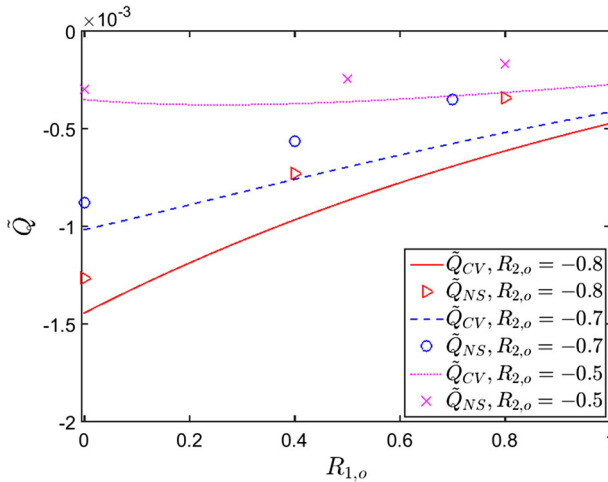
Fig. 8 $\tilde{Q}$ versus $R_{1,o}$ as $M \to \infty$. The *curves* represent different values of $R_{2,o}$. All data have the same parameter values of $\tilde{a} = 1/6$, $\tilde{b}_i = 2/3$, $\tilde{k} = \pi/500$, and $R_{1,i} = R_{2,i} = 0$

with an increase in the ABM gap thickness (i.e. thickening) can result in reduced reverse transport in the ABM.

In Fig. 9b we investigate the changes in $\tilde{Q}$ when the wave amplitude, $\tilde{a}$, is reduced. Here, it is observed that when $\tilde{a}$ decreases, the magnitude of fluid volume transported, $\left|\tilde{Q}\right|$, also decreases. This is expected because the boundary wave provides the force that drives the flow, for both the forward and reverse directions. Thus, a smaller $\tilde{a}$ is equivalent to a weaker driving force, which in turn decreases the flow magnitude. For an aging brain, this implies that when the arterial wall stiffens, the wave amplitude of the cardiac pulsation is weaker and reduces the amount of solutes that can be transported through the ABM.

In Fig. 9c both thickening and stiffening of the ABM are considered simultaneously. The combinatorial aging effect indicates a dramatic decrease in the net flow magnitude, especially for the range of $R_{2,o}$ where reverse transport occurs. We also analyzed the effects of decreasing $\tilde{b}_i$ for $R_{1,o} > 0$ and $M \to \infty$, as shown in Fig. 11. The results are similar to those seen in Fig. 9a; in particular, the overall reverse flow decreases with decreasing $\tilde{b}_i$.

3.5 Statements on the control volume analysis

Figures 5, 6, 8, 9, and 11 show that $\tilde{Q}_{CV}$ and $\tilde{Q}_{NS}$ have the same order of magnitude and follow the same trend. The differences between $\tilde{Q}_{CV}$ and $\tilde{Q}_{NS}$ are mainly attributed to the assumptions we make in the control volume analysis. First, we considered only the two leading order terms in the binomial expansions since we expect the contributions of the subsequent terms to diminish. Secondly, we assumed the spatially-averaged velocity, over one wavelength, is approximately equivalent to the time-averaged velocity at $x = 0$ over one wave period.
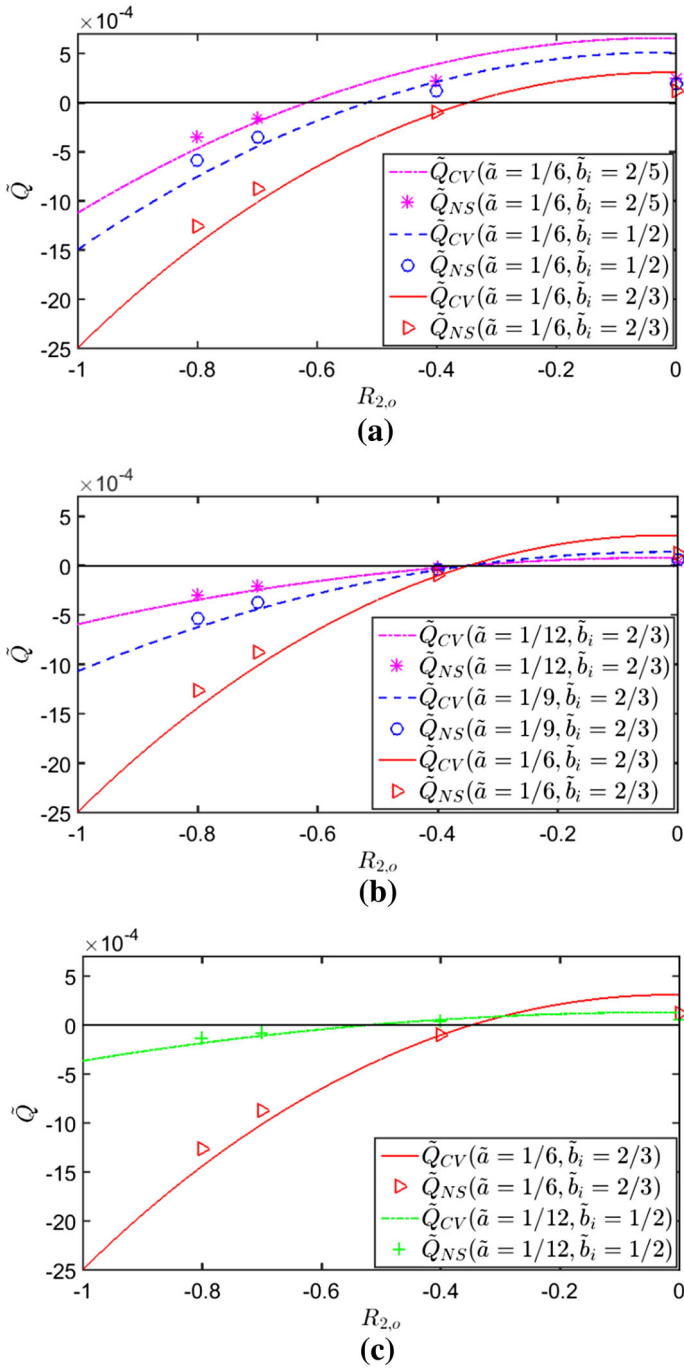
Fig. 9 $\tilde{Q}$ versus $R_{2,o}$ under three different aging conditions. All computation are conducted under $M = 1$, $R_{2,i} = 0$, and $\tilde{k} = \pi/500$. **a** Changing the ABM thickness, $\tilde{b}_i$, while maintaining the ABM stiffness, $\tilde{a}$; **b** changing the value of $\tilde{a}$ while keeping $\tilde{b}_i$ constant; **c** simultaneously decreasing $\tilde{b}_i$ and $\tilde{a}$
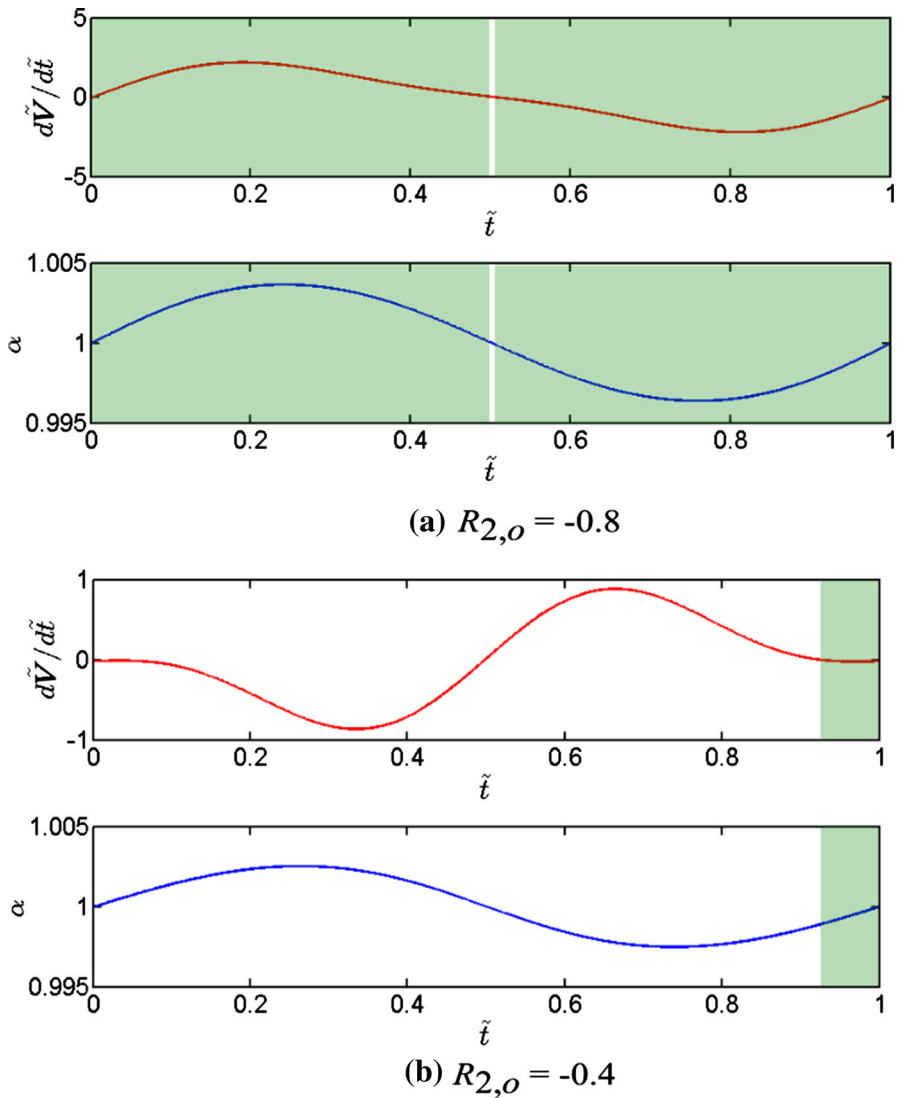
Fig. 10 $d\tilde{V}/d\tilde{t}$ verses $\tilde{t}$ and α verses $\tilde{t}$ with $M = 1$, $R_{2,i} = 0$, $\tilde{a} = 1/6$, $\tilde{b}_i = 1/2$, and $\tilde{k} = \pi/500$. **a** $R_{2,o} = -0.8$; **b** $R_{2,o} = -0.4$. The *shaded* regions indicate the time intervals of favorable conditions for reverse flow

Nevertheless, the control volume approach yields good prediction of flow direction while needing only a very small fraction of the computational time for obtaining numerical solutions of the Navier–Stokes equations. With the computational hardware available to us, the amount of time needed to calculate $\tilde{Q}_{CV}$ for $M = 1$, $R_{2,i} = 0$, $R_{2,o} = -0.8$, $\tilde{a} = 1/6$, $\tilde{b}_i = 2/3$, and $\tilde{k} = \pi/500$ was approximately 0.1 seconds, while the amount of time to calculate $\tilde{Q}_{NS}$ using the same parameter values is approximately 4.5 h. Thus, the control volume analysis offers a tool that allows a researcher

to rapidly survey the parameter space to elucidate the conditions necessary for reverse flow.

4 Concluding remark

To date, the exact mechanisms of how A β is cleared from a healthy brain and is accumulated in an aging brain remain elusive. Current opinions in the medical field suggest that an understanding of A β clearance not only offers insights into the development and progression of Alzheimer's disease, but also may suggest potential treatment options to slow down or reverse its adverse effects. In this paper, we report on a boundary wave-driven hydrodynamic mechanism that is a potential candidate for explaining A β clearance in the ABM as reported in literature. What makes this mechanism a good candidate is that we are able to incorporate critical physiological conditions into our model and obtain transport results that are qualitatively in agreement with clinical and experimental observations reported in literature.

Through our numerical studies, we found that forward-propagating and reflected boundary waves can influence the direction of fluid transport in an ABM that is modeled as an annulus. This is despite the fact that the blood flow, due to cardiac pulsations, propagates only in the forward direction and is the driving force of transport in the ABM. Several parameters associated with the boundary waves and the annular geometry are found to be critically important in determining the transport direction, including the change of arterial stiffness at arterial bifurcation sites (manifested through the wave reflection coefficients), basement membrane thickness, wavelength, and ABM stiffness (manifested through wave amplitude). We also found that slight changes in these parameters for an aging brain can lead to dramatic changes in transport direction and
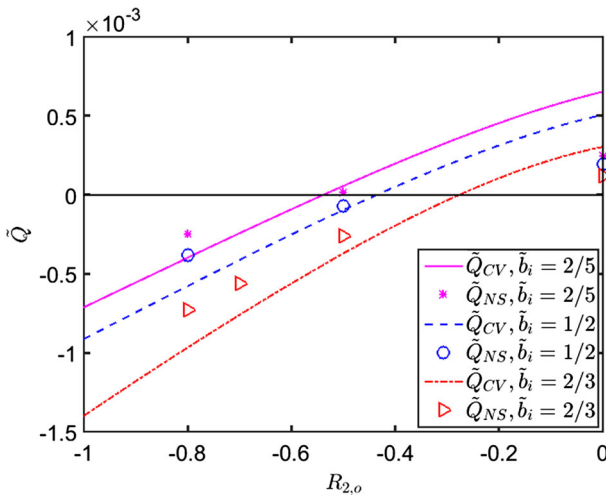
Fig. 11 $\tilde{Q}$ versus $R_{2,o}$ under different values of the ABM thickness, $\tilde{b}_i$, while maintaining the ABM stiffness $\tilde{a} = 1/6$. All computation are conducted under $M \to \infty$, $R_{1,o} = 0.4$, $R_{1,i} = R_{2,i} = 0$ and $\tilde{k} = \pi/500$

magnitude. This offers a potential explanation of the biomechanical causes of Aβ clearance failure in the ABM found in Alzheimer's disease patients.

Finally, the preferential transport theory presented in this manuscript does not presume contraction of the smooth muscle cells as the main boundary deformation mechanism. Rather, the arterial wall deformation is assumed to be purely linked to the cardiac pulsations. Iliff et al. (2013) report on wave pulsations along brain penetrating arteries/arterioles (at length scales similar to our study). While it is likely that cardiac pulsations diminish at the pre-capillary level, cardiac pulsations in small arteries/large arterioles exist and can still serve as the driving force for a reverse flow in the ABM (i.e. to satisfy continuity in one continuous flow conduit). Therefore our preferential transport theory does not require cardiac pulsations at the capillary and/or pre-capillary arteriole level. To drive flow, cardiac pulsations are only necessary at the level of the small arteries/large arterioles.

5 Appendix 1: Momentum correction factor for an annulus

The dimensionless momentum-flux correction factor at a control surface k is

$$\beta_k = \frac{1}{A_k} \int_{A_k} \left(\frac{u_k}{\bar{u}_k} \right)^2 dA_k \tag{13}$$

where u_k is the velocity profile at the control surface. $\beta_k = 1$ represents a uniform flow profile while a parabolic flow profile leads to $\beta_k > 1$. The velocity profile for a steady, incompressible, laminar, unidirectional flow in an annulus with no-slip boundary conditions is

$$u_k(r) = \frac{r_{i,k}^2 - r_{o,k}^2}{4\mu} \frac{dp}{dx} \left(\frac{r^2 - r_{o,k}^2}{r_{i,k}^2 - r_{o,k}^2} - \frac{\ln\left(\frac{r}{r_{o,k}}\right)}{\ln\left(\frac{r_{i,k}}{r_{o,k}}\right)} \right) \tag{14}$$

where dp/dx is the local pressure gradient and μ is the fluid viscosity, and

$$\begin{aligned}
\bar{u}_k &= -\frac{1}{2\mu} \frac{dp}{dx} \int_{r_{i,k}}^{r_{o,k}} \left(\frac{r^2 - r_{o,k}^2}{r_{i,k}^2 - r_{o,k}^2} - \frac{\ln\left(\frac{r}{r_{o,k}}\right)}{\ln\left(\frac{r_{i,k}}{r_{o,k}}\right)} \right) r \, dr \\
&= -\frac{1}{8\mu} \frac{dp}{dx} \left(r_{i,k}^2 + r_{o,k}^2 - \frac{r_{i,k}^2 - r_{o,k}^2}{\ln\left(\frac{r_{i,k}}{r_{o,k}}\right)} \right).
\end{aligned} \tag{15}$$

6 Appendix 2: Derivation of the control volume flow rate formula

Equation ([8](#)) can be re-written in terms of $\bar{u}_2$ and α,

$$\bar{u}_2 = \pm \bar{u}_1 \left(\frac{1}{\alpha}\right)^{\frac{1}{2}} \left(1 - \frac{1}{\bar{u}_1^2 \beta_1 A_1} \frac{dP}{dt}\right)^{\frac{1}{2}}, \tag{16}$$

where $\bar{u}_2$ must remain real at all times and requires $dP/dt < \bar{u}_1^2 \beta_1 A_1$. The periodic nature of the rate of change of momentum in the control volume allows us to infer that $|dP/dt| < \bar{u}_1^2 \beta_1 A_1$. We thus employ a binomial expansion of Eq. ([16](#)),

$$\bar{u}_2 = \pm \bar{u}_1 \left(\frac{1}{\alpha}\right)^{1/2} \left[1 - \frac{1}{2}\left(\frac{1}{\bar{u}_1^2 \beta_1 A_1} \frac{dP}{dt}\right) - \frac{1}{8}\left(\frac{1}{\bar{u}_1^2 \beta_1 A_1} \frac{dP}{dt}\right)^2 + \cdots\right]. \tag{17}$$

Since at any given instant of time a velocity must be unique, we determine the sign in Eq. ([17](#)) by considering the leading order term and substitute it into Eq. ([7](#)), which leads to

$$\bar{u}_1 = \frac{dV}{dt} \frac{1}{A_1} \frac{1}{1 \mp \alpha^{1/2}}. \tag{18}$$

The minus sign solution in Eq. ([18](#)) is physically unreasonable because during each deformation cycle, there must exist instances when $\alpha = 1$. Thus, at those instances

$$\lim_{\alpha=1} \frac{1}{1 - \alpha^{1/2}} \to \infty$$

which leads to singularity for $\bar{u}_1$. This indicates that the only plausible sign for Eq. ([17](#)) must be negative and

$$\bar{u}_2 = -\bar{u}_1 \left(\frac{1}{\alpha}\right)^{1/2} \left[1 - \frac{1}{2}\left(\frac{1}{\bar{u}_1^2 \beta_1 A_1} \frac{dP}{dt}\right) - \frac{1}{8}\left(\frac{1}{\bar{u}_1^2 \beta_1 A_1} \frac{dP}{dt}\right)^2 + \cdots\right]. \tag{19}$$

When the two leading order terms in Eq. ([19](#)) are considered and substituted into Eq. ([7](#)), it yields a quadratic equation in terms of $\bar{u}_1$,

$$\left(1 + \alpha^{1/2}\right) A_1 \bar{u}_1^2 - \left(\frac{dV}{dt}\right) \bar{u}_1 - \frac{1}{2\beta_1} \alpha^{1/2} \frac{dP}{dt} = 0, \tag{20}$$

whose solution is

$$\bar{u}_1 = \frac{\left(\frac{dV}{dt}\right) \pm \sqrt{\left(\frac{dV}{dt}\right)^2 - 2\frac{A_1}{\beta_1} \frac{dP}{dt} \left(1 + \alpha^{1/2}\right)}}{2\left(1 + \alpha^{1/2}\right) A_1}. \tag{21}$$

Again, $\bar{u}_1$ must remain real at all times, and given the periodic nature of dP/dt, we can infer that

$$\left| 2 \frac{A_1}{\beta_1} \left(\frac{dV}{dt} \right)^{-2} \frac{dP}{dt} \left(1 + \alpha^{1/2} \right) \right| \le 1. \tag{22}$$

Once again by invoking the binomial series expansion of the square root term in Eq. (21) and keeping the two leading order terms, we get

$$\bar{u}_1 \approx \frac{\left(\frac{dV}{dt} \right) \pm \left(\frac{dV}{dt} \right) \left[1 + \frac{A_1}{\beta_1} \frac{dP}{dt} \left(\frac{dV}{dt} \right)^{-2} \left(\alpha + \alpha^{1/2} \right) \right]}{2 \left(1 + \alpha^{1/2} \right) A_1}. \tag{23}$$

Numerical evaluation of Eq. (23) requires us to obtain an approximate expression for dP/dt. We define a spatially averaged velocity in the x-direction as $u_{avg,S} = (1/V) \int \int \int (\mathbf{u} \cdot \hat{x}) dV = P/V$ where $\mathbf{u}$ is velocity field vector and $\hat{x}$ is the unit direction vector pointing in the axial direction. Since the flow is periodic, a velocity averaged over a space of one wavelength is approximately equal to a timed-averaged velocity $u_{avg,T}$ at A_1 over one period, or

$$u_{avg,S} \approx u_{avg,T} = \frac{1}{\tau} \int_0^\tau \bar{u}_1(t) \, dt = \frac{Q_{CV}}{\int_0^\tau A_1(t) \, dt}. \tag{24}$$

Given that $u_{avg,T}$ is not a function of time,

$$\frac{dP}{dt} = \frac{d}{dt} \left(u_{avg,S} V \right) \approx \frac{d}{dt} \left(u_{avg,T} V \right) = \frac{Q_{CV}}{\int_0^\tau A_1(t) \, dt} \frac{dV}{dt}. \tag{25}$$

Substituting Eq. (25) into Eq. (23) yields

$$Q_{CV} \approx \int_0^\tau \frac{dV}{dt} \frac{1}{2 \left(1 + \alpha^{1/2} \right)} dt$$

$$\pm \int_0^\tau \frac{1}{2 \left(1 + \alpha^{1/2} \right)} \left[\frac{dV}{dt} + \frac{A_1}{\beta_1} \frac{Q_{CV}}{\int_0^\tau A_1(t) \, dt} \left(\alpha + \alpha^{1/2} \right) \right] dt. \tag{26}$$

Equation (26) shows two possible solutions for Q_{CV}, which also must be unique. We first consider Eq. (26) with the negative sign, which yields

$$Q_{CV} = - \int_0^\tau \left[\frac{A_1}{2\beta_1 \left(1 + \alpha^{1/2} \right)} \frac{Q_{CV} \left(\alpha + \alpha^{1/2} \right)}{\int_0^\tau A_1(t) \, dt} \right] dt$$

$$= - \frac{Q_{CV}}{2\beta_1 \int_0^\tau A_1(t) \, dt} \int_0^\tau A_1 \alpha^{1/2} dt. \tag{27}$$

Rearranging Eq. (27) leads to $Q_{CV} = 0$, regardless of the annular deformation, which is not physically plausible given that a periodically deforming control volume

due to traveling boundary waves should result in non-zero overall flow. Choosing the positive sign in Eq. (26) thus leads to Eq. (7).

References

Abbott NJ (2004) Evidence for bulk flow of brain interstitial fluid: significance for physiology and pathology. Neurochem Int 45(4):545–552

Alastruey J, Parker KH, Sherwin SJ (2012) Arterial pulse wave haemodynamics. In: Anderson. 11th international conference on pressure surges, pp 401-442

Alzheimer's Association (2010) 2010 Alzheimer's disease facts and figures. Alzheimer's Dement 6(2):158-194

Bilston L, Flecther D, Brodbelt A, Stoody M (2003) Arterial pulsation-driven cerebrospinal fluid flow in the perivascular space: a computational model. Comput Methods Biomech Biomed Eng 6(4):235–241

Carare RO, Bernardes-Silva M, Newman T, Newman T, a, Page a M, Nicoll J a R, Perry VH, Weller RO (2008) Solutes, but not cells, drain from the brain parenchyma along basement membranes of capillaries and arteries: significance for cerebral amyloid angiopathy and neuroimmunology. Neuropathol Appl Neurobiol 34(2):131–144

Elmore WC, Heald MA (1969) Physics of waves. Courier Corporation, New York

Farkas E, Luiten PG (2001) Cerebral microvascular pathology in aging and Alzheimer's disease. Prog Neurobiol 64(6):575–611

Fung YC (1984) Biodynamics circulation. Springer, New York

Hawkes CA, Hartig W, Kacza J, Schliebs R, Weller RO, Nicoll JA, Carare RO (2011) Perivascular drainage of solutes is impaired in the ageing mouse brain and in the presence of cerebral amyloid angiopathy. Acta Neuropathol 121(4):431–443

Hawkes CA, Gatherer M, Sharp MM, Dorr A, Yuen HM, Kalaria R, Weller RO, Carare RO (2013) Regional differences in the morphological and functional effects of aging on cerebral basement membranes and perivascular drainage of amyloid- from the mouse brain. Aging cell 12(2):224–236

Hughes TM, Kuller LH, Barinas-Mitchell EJ, McDade EM, Klunk WE, Cohen AD, Mathis CA, DeKosky ST, Price JC, Lopez OL (2014) Arterial stiffness and beta-amyloid progression in nondemented elderly adults. JAMA Neurol 71(5):562–568

Iliff JJ, Wang MH, Liao YH, Plog BA, Peng WG, Gundersen GA, Gundersen GA, Benveniste H, Vates GE, Deane R, Goldman SA, Nagelhus EA, Nedergaard M (2012) A paravascular pathway facilitates CSF flow through the brain parenchyma and the clearance of interstitial solutes, including amyloid beta. Sci Transl Med 4(147):147ra111

Iliff JJ, Wang MH, Zeppenfeld DM, Venkataraman A, Plog BA, Liao YH, Deane R, Nedergaard M (2013) Cerebral arterial pulsation drives paravascular CSF-interstitial fluid exchange in the murine brain. J Neurosci 33(46):18190–18199

Kamath S (1981) Observations on the length and diameter of vessels forming the circle of Willis. J Anat 133(3):419–423

Knopf PM, Cserr HF, Nolan SC, Wu TY, Harlingberg CJ (1995) Physiology and immunology of lymphatic drainage of interstitial and cerebrospinal-fluid from the brain. Neuropathol Appl Neurobiol 21(3):175–180

Krings T, Mandell DM, Kiehl TR, Geibprasert S, Tymianski M, Alvarez H, terBrugge KG, Hans FJ (2011) Intracranial aneurysms: from vessel wall pathology to therapeutic approach. Nat Rev Neurol 7(10):547–559

Li JK (2004) Dynamics of the vascular system. World Scientific, Singapore

Mawuenyega KG, Sigurdson W, Ovod V, Munsell L, Kasten T, Morris JC, Yarasheski KE, Bateman RJ (2010) Decreased clearance of CNS beta-amyloid in Alzheimer's disease. Science 330(6012):1774–1774

Nichols WW (2005) Clinical measurement of arterial stiffness obtained from noninvasive pressure waveforms. Am J Hypertens 18(1):3S–10S

Nichols W, O'Rourke M, Vlachopoulos C (2011) McDonald's blood flow in arteries: theoretical, experimental and clinical principles. CRC Press, Boca Raton

Papageorgiou GL, Jones BN, Redding VJ, Hudson N (1990) The area ratio of normal arterial junctions and its implications in pulse waves. Cardiovasc Res 24(6):478–484

Preston SD, Steart PV, Wilkinson A, Nicoll JAR, Weller RO (2003) Capillary and arterial cerebral amyloid angiopathy in Alzheimer's disease : defining the perivascular route for the elimination of amyloid beta from the human brain. Neuropathol Appl Neurobiol 29(2):106–118

Schley D, Carare-Nnadi R, Please CP, Perry VH, Weller RO (2006) Mechanisms to explain the reverse perivascular transport of solutes out of the brain. J Theor Biol 238(4):962–974

Tanzi RE, Moir RD, Wagner SL (2004) Clearance of Alzheimer's A beta peptide: the many roads to perdition. Neuron 43(5):605–608

Wang P, Olbricht WL (2011) Fluid mechanics in the perivascular space. J Theor Biol 274(1):52–57

Weller R, Subash M, Preston S, Mazanti I, Carare R (2008) Perivascular drainage of amyloid-β peptides from the brain and its failure in cerebral amyloid angiopathy and Alzheimer's disease. Brain Pathol 18:253–266

Weller RO, Galea I, Carare RO, Minagar a (2010) Pathophysiology of the lymphatic drainage of the central nervous system: implications for pathogenesis and therapy of multiple sclerosis. Pathophysiology 17(4):295–306

Yang ST, Mayhan WG, Faraci FM, Heistad DD (1991) Endothelium-dependent responses of cerebral blood-vessels during chronic hypertension. Hypertension 17(5):612–618

Yao W, Li YB, Ding GH (2012) Interstitial fluid flow: the mechanical environment of cells and foundation of Meridians. Evid Based Complement Alternat Med 2012:853516. doi:10.1155/2012/853516